Science Arts & Métiers (SAM)
is an open access repository that collects the work of Arts et Métiers Institute of Technology researchers and makes it freely available over the web where possible.

This is an author-deposited version published in: https://sam.ensam.eu
Handle ID: .http://hdl.handle.net/10985/10734

**To cite this version :**

Pierric MORA, Eric DUCASSE, Marc DESCHAMPS - Transient 3D elastodynamic field in an embedded multilayered anisotropic plate - Ultrasonics - Vol. 69, p.106-115 - 2016

Any correspondence concerning this service should be sent to the repository Administrator : scienceouverte@ensam.eu

# Transient 3D elastodynamic field in an embedded multilayered anisotropic plate

**Pierric Mora**[1] pierric.mora@u-bordeaux.fr

**Eric Ducasse**[1,3,4] eric.ducasse@u-bordeaux.fr

**Marc Deschamps**[1,2] marc.deschamps@u-bordeaux.fr

[1] Univ. Bordeaux, $I_2M-APy$, UMR 5295, F-33400 Talence, France.

[2] CNRS, $I_2M-APy$, UMR 5295, F-33400 Talence, France.

[3] Arts et Metiers ParisTech, $I_2M-APy$, UMR 5295, F-33400 Talence, France.

[4] Corresponding author. Tel. +33(0)540003138. Fax +33(0)540006964.

## Abstract

The aim of this paper is to study the ultrasonic response to a transient source that radiates ultrasonic waves in a 3D embedded multilayered anisotropic and dissipative plate. The source can be inside the plate or outside, in a fluid loading the plate for example. In the context of *Non-Destructive Testing* applied to composite materials, our goal is to create a robust algorithm to calculate ultrasonic field, irrespective of the source and receiver positions.

The principle of the method described in this paper is well-established. This method is based on time analysis using the Laplace transform. In the present work, it has been customized for computing ultrasonic source interactions with multilayered dissipative anisotropic plates. The fields are transformed in the 2D Fourier wave-vector domain for the space variables related to the plate surface, and they are expressed in the partial-wave basis. Surprisingly, this method has been very little used in the ultrasonic community, while it is a useful tool which complements the much used technique based on generalized Lamb wave decomposition. By avoiding mode analysis – which can be problematic in some cases – *exact numerical* calculations (*i.e.*, approximations by truncating infinite series that may be poorly convergent are not needed) can be made in a relatively short time for immersed plates and viscoelastic layers. Even for 3D cases, numerical costs are relatively low. Special attention is given to separate up- and down-going waves, which is a simple matter when using the Laplace transform.

Numerical results show the effectiveness of this method. Three examples are presented here to investigate the quality of the model and the robustness of the algorithm: first, a comparison of experiment and simulation for a monolayer carbon-epoxy plate, where the diffracted field is due to a source located on the first free surface of the sample, for both dissipative and non-dissipative cases; second, the basic configuration of an aluminum plate immersed in water has been chosen to study wave propagation in ZGV (Zero Group Velocity) conditions; finally, a 2D plate consisting of 8 stacked carbon-epoxy layers immersed in water is treated, with a source located inside the plate, distributed in depth and extending over four layers.

## Highlights

- Transient response computation of a 3D embedded multilayered anisotropic plate.
- Ultrasonic field calculation, irrespective of the source and receiver positions.
- Standard numerical integral transform may provide a fast and efficient tool.
- Up- and down-going waves are easily selected when using the Laplace transform.

## Keywords

Embedded multilayered plate ; Transient ultrasonic response ; Partial-wave expansion ; Integral transform domain ; Numerical inverse Laplace transform

PACS 43.20.Bi ; 43.20.Mv

# 1 Introduction

The study of diffraction of acoustic waves in laminated plates has interested the communities of geophysics, underwater acoustics and non-destructive testing for several decades.

Numerous practical approaches exist today to calculate the response of these media to different sources. The choice of method used is governed by the situation under consideration. For instance, the aim may be near-field calculation or far-field calculation, the responses may be needed in the time or the frequency domain, the guides may or may not be loaded, *etc.* Expanding the solution in terms of normal modes in the frequency domain is one of the best-known methods. The modes correspond to generalized Lamb waves for laminated plates, and can be obtained numerically in different ways, by searching for the roots of the determinant of a matrix [14], or by obtaining the eigenvalues of a finite-element matrix (*e.g.*, [13, 8]).

This modal method is well-suited to deal with calculations in the far-field domain for guides in vacuum. This is because in the far field the modes are well-built, and only a limited number of them, *i.e.*, the propagative modes, contribute, which makes modal theory very efficient. For plates in vacuum, the solution can also be expanded in terms of modes in the time domain, after performing a Fourier transform with respect to the horizontal coordinates (in the plane of the plate) [12, 7], assuming that the source is bounded and bandlimited in horizontal wavenumber, according to the Nyquist-Shannon sampling theorem. This second method is more suitable than the first one for 3D calculations in anisotropic media because it does not make use of an angular integration variable, nor is the direction of propagation of the modes required [26].

However, for loaded plates (*i.e.*, plates immersed or embedded in an unbounded medium), modes do not constitute a complete basis, which makes modal expansion theoretically more delicate, if not impossible. Furthermore, it is still a challenge to build a robust and accurate algorithm to obtain the modes numerically. Indeed, exact eigenvalue statements have been proposed only in some restricted cases [9]. For more general situations, PML [4] are sometimes chosen for modeling the unbounded layers, but are well-known to be problematic in the case of backward propagative modes and may also lead to instabilities for anisotropic media. So, in this case this modal technique must be used with some caution.

To avoid difficulties due to radiation into half-space(s), different approaches have been developed. Park and Kausel [17, 18] have shown that, for loaded guides, it is possible to get an exact solution from the modal basis obtained for guides in vacuum. The influence of the two semi-infinite media is taken into account by two secondary source terms applied on both supposedly free surfaces. The amplitude of each mode is then

determined by solving a Volterra integral equation. However, this method, the so-called "Substructure Method", exhibits poor convergence and problems of instability [17, 18].

An alternative to the modal theory consists in conserving the initial integral instead of expressing it as a sum of modes by using the residue theorem. The problem is then to calculate this integral correctly, knowing that sampling the integration path, which is close to the poles, can produce numerical errors. To this end, in the case of a stack of 3D isotropic plate layers, in 1965, Phinney [19] proposed to deform the integration path of the Fourier integral on frequency in the complex plane by adding an arbitrary imaginary part to the frequency. The choice of the arbitrary constant has been studied by Kausel and Roësset [11] in order to increase the accuracy of the numerical inverse transform involved to come back to the time domain. This method can be found in the literature under the name of Exponential Window Method. Although it is never stated explicitly, all the numerical inversions related to the Exponential Window Method give causal signals and correspond to the inverse Laplace transform defined by the Bromwich contour. The same idea has been used to deal with wave diffraction in 3D isotropic dissipative (or non-dissipative) plates [28]. This work has been extended to model ultrasound generation by laser in 2D dissipative anisotropic plates by Audoin and Guilbaud [1].

Curiously, to our knowledge, this causal non-modal technique is used relatively infrequently by the mechanics community, even though it is able to solve complex cases while insuring a perfect control and competitive numerical cost towards the modal methods. This is probably because it is a purely numerical technique, for which the physical meaning contained in modal theory is lost. If a precise physical interpretation of diffracted wavefronts is needed, both modal and non-modal approaches are then necessary.

In this paper we propose to study the ultrasonic response to a transient source that radiates ultrasonic waves in a 3D embedded multilayered anisotropic and dissipative plate. The source can be inside the plate or outside, in a fluid loading the plate for example. In some way, the goal of this paper is to give to this well-established non-modal method a larger diffusion among the ultrasonic community. The examples presented here are chosen to cover a broad range of situations of *Non-Destructive Testing* (NDT) of plates, with a special focus on composite plates, considering guided wave as well as bulk wave regimes. The formalism may be readily applied to write a robust and versatile algorithm to calculate ultrasonic field, irrespective of the source and receiver positions. The fields are transformed in the Laplace domain for the time variable and in the 2D Fourier wave-vector domain for the space variables related to the horizontal plate surface, assuming that the source is bounded and bandlimited in horizontal wavenumber, according to the Nyquist-Shannon sampling theorem. Working in the Laplace domain gives access to all the general theorems associated to this transformation and specifically related to causal signals. Beyond the specific interest of this paper, this can be useful for building solutions to many other problems.

After a brief description of the basic equations (Section 3), described with our notations, the solution is obtained in the 3D transformed-domain. Special attention is given to separate up- and down-going waves, which is a simple matter when using the Laplace transform. Section 4 is devoted to numerical results. First, for a monolayer carbon-epoxy plate, the diffracted field due to a source located on the first free surface of the sample is calculated for both dissipative and non-dissipative cases. The waveforms are then successfully compared with some experiments. Second, for an aluminum plate immersed in water: this very basic configuration has been chosen to study wave propagation in ZGV (Zero Group Velocity) conditions. Finally, a 2D plate consisting of 8 stacked carbon-epoxy layers immersed in water is treated to investigate the quality of the model and the robustness of the algorithm. The 2D source is located inside the plate and extends over four layers.

| | Time-domain $t$ | notation | Laplace-domain $s$ | notation |
|---|---|---|---|---|
| Physical space $\mathbf{x}, z$ | $(\mathbf{x}, z, t)$ | $\mathbf{u}$ | $(\mathbf{x}, z, s)$ | $\mathbf{U}$ |
| Horizontal wave vector $\mathbf{k}$<br>Vertical position $z$ | $(\mathbf{k}, z, t)$ | $\tilde{\mathbf{u}}$ | $(\mathbf{k}, z, s)$ | $\tilde{\mathbf{U}}$ |
| Horizontal wave vector $\mathbf{k}$<br>Vertical wavenumber $k_z$ | $(\mathbf{k}, k_z, t)$ | $\hat{\mathbf{u}}$ | $(\mathbf{k}, k_z, s)$ | $\hat{\mathbf{U}}$ |

Table 1: Notations

# 2 Notations

The vector $\mathbf{x} = (x, y)$ will denote spatial coordinates in the $xy$-plane. The associated planar wave-vector in the Fourier space will be denoted by $\mathbf{k} = (k_x, k_y)$. In the time domain, all fields are denoted with lower case letters, whereas in the Laplace domain capital letters are used. Symbols are added to indicate a Fourier transform over the space variables. These conventions are summarized in Table 1. The fields $\mathbf{u}$, $\boldsymbol{\sigma}_z$, $\boldsymbol{\eta}$, $\mathbf{f}_\beta$, $\boldsymbol{\sigma}_\beta$ that are introduced later follow the same rules: they will be denoted $\tilde{\mathbf{U}}$, $\tilde{\boldsymbol{\Sigma}}_z$, $\tilde{\mathbf{H}}$, $\tilde{\mathbf{F}}_\beta$, $\tilde{\boldsymbol{\Sigma}}_\beta$ in the $(\mathbf{k}, z, s)$ dual space. The dependence of these fields along the space and spectral variables will be made explicit only when necessary.

The mechanical properties $\rho_\beta$ and $c^{\beta}_{ijkm}$ are constant in each layer. Notice that the $z$ axis is taken positive downwards, and that therefore an "upgoing" (*resp.* "downgoing") wave propagates towards decreasing (*resp.* increasing) $z$.

# 3 Equations and background

Let us consider a multilayered medium made of a plate system consisting of a number $N$ of perfect flat layers of normal $\mathbf{n}$ along $z$-axis, stacked together. The layers are labeled $\beta$. The interface between layers $\beta$ and $\beta$+1, also labeled $\beta$, is located at position $z = z_\beta$, as illustrated in Fig. 1. Each layer is an anisotropic solid, with a given thickness $h_\beta = z_\beta - z_{\beta-1}$. The areas above and below this plate system can either be vacua or semi-infinite half-spaces of solid (or fluid) media. The plate is assumed to be infinite in the $xy$-plane This stratified medium is submitted to external forces that can be located anywhere. The first interface ($\beta = 0$) is always located at $z_0 = 0$.

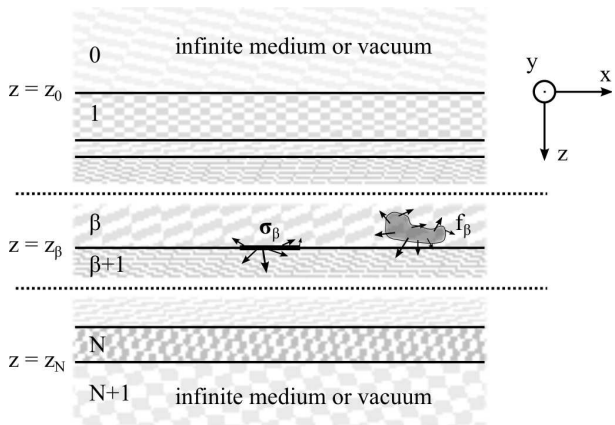


Figure 1: A multilayered infinite plate of $N$ different layers.

## 3.1 Basic equations in the physical space

With our notations, let us first state the wave equations in each layer. Combining Newton's second law, the causality principle and Hooke's law, the displacement field $\mathbf{u}(\mathbf{x}, z, t)$ is given, at any time $t$ and any location $(\mathbf{x}, z)$, by the following system expressed in the medium $\beta$:

$$\left\{ \begin{array}{ll} \rho_\beta\, \partial_t^2 \mathbf{u}(\mathbf{x}, z, t) - (\bigtriangledown \overset{\beta}{\diamond} \bigtriangledown)\, \mathbf{u}(\mathbf{x}, z, t) = \mathbf{f}_\beta(\mathbf{x}, z, t), & \text{for } t > 0, \\ \mathbf{u}(\mathbf{x}, z, t) = 0, & \text{for } t < 0, \\ \boldsymbol{\sigma}_z(\mathbf{x}, z, t) = (\mathbf{n} \overset{\beta}{\diamond} \bigtriangledown)\, \mathbf{u}(\mathbf{x}, z, t), & \end{array} \right. \tag{1}$$

where the quantity $\boldsymbol{\sigma}_z(\mathbf{x}, z, t)$ expresses the stress in the $z$-direction (normal to the interfaces) and $\rho_\beta$ stands for the mass density. The bilinear product $\overset{\beta}{\diamond}$ has been defined in [6] by a three-by-three matrix $(\mathbf{a} \overset{\beta}{\diamond} \mathbf{b})$ such that $(\mathbf{a} \overset{\beta}{\diamond} \mathbf{b})_{im} = c^{\beta}_{ijkm}\, a_j\, b_k$, with the Einstein summation convention. The above equations depend on each layer through the values of the elastic constants $c^{\beta}_{ijkm}$, *i.e.* through the operator $\overset{\beta}{\diamond}$. The field $\mathbf{f}_\beta(\mathbf{x}, z, t)$ denotes the force per unit volume exerted by the part of the sources located in layer $\beta$.

Continuity equations at the interface $\beta$ are given by the following system:

$$\begin{pmatrix} \mathbf{u}(\mathbf{x}, z_\beta^+, t) \\ \boldsymbol{\sigma}_z(\mathbf{x}, z_\beta^+, t) \end{pmatrix} - \begin{pmatrix} \mathbf{u}(\mathbf{x}, z_\beta^-, t) \\ \boldsymbol{\sigma}_z(\mathbf{x}, z_\beta^-, t) \end{pmatrix} = \begin{pmatrix} \mathbf{0} \\ \boldsymbol{\sigma}_\beta(\mathbf{x}, t) \end{pmatrix}, \tag{2}$$

where $z_\beta^-$ and $z_\beta^+$ indicate the fact that the field under consideration is calculated in layers $\beta{-}1$ and $\beta$, respectively. The *interface source term* $\boldsymbol{\sigma}_\beta(\mathbf{x}, t)$ defines the normal stress jump at interface $\beta$, and corresponds to an applied force per unit surface if one of the media is a vacuum. Notice that if $\boldsymbol{\sigma}_\beta = \mathbf{0}$, then Eq. (2) merely expresses the continuity of displacement and normal stress.

For simplicity, the $\beta$ index will be omitted below and will be reintroduced only when necessary to avoid ambiguity. The volumic sources described by $\mathbf{f}_\beta(\mathbf{x}, z, t)$ in Eq. (1) can straddle two or more layers. In such case, the volumic source term is considered as zero at each interface ($z = z_\beta$).

Eq. (1) and (2) are to be solved using Fourier and Laplace transforms on invariant dimensions. In a first time (see sections 3.2 and 3.3), Eq. (1) is solved separately in each layer containing a source term. This defines an *incident field* in each layer, which corresponds to the field that a source would radiate in this layer considered to be unbounded. Then (see section 3.4), the *reflected field* can be obtained, which is the contribution of all the interfaces, and is calculated by taking into account the continuity relationships of Eq. (2). In this article, the so-called *Global matrix* (*e.g.*, [14]) method is adopted to perform the latter operation. The *total field* is finally obtained as the sum of the *incident* and *reflected* fields.

## 3.2 Separation of up- and down-going waves

The aim of this section is to emphasize that up- and down-going bulk waves, which are the solutions of Christoffel's equation, are easily separated in the Laplace domain. It may be skipped in a first reading.

Let us apply a 3D Fourier transform to the space variables to Eq. (1). The space domain $(\mathbf{x}, z)$ is then transformed into the spectral domain defined by $\mathbf{K} = (\mathbf{k}, k_z)$, where $\mathbf{K}$ stands for the wave vector. This yields the following differential equation:

$$\rho\, \partial_t^2 \hat{\mathbf{u}}\,(t) + (\mathbf{K} \diamond \mathbf{K})\, \hat{\mathbf{u}}\,(t) = \hat{\mathbf{f}}\,(t)\,. \tag{3}$$

If $\mathbf{K} = \mathbf{0}$, which corresponds to the rigid body motion, then $\hat{\mathbf{u}} = \rho^{-1}\, \mathbb{r} * \hat{\mathbf{f}}$, where $\mathbb{r}$ denotes the ramp function and the operator $*$ is the time convolution product. If $\mathbf{K} \neq \mathbf{0}$, the matrix $(\mathbf{K} \diamond \mathbf{K})$ is then real-valued symmetric

positive-definite, and therefore admits three positive eigenvalues $\rho\,\omega_i^2$ with associated eigenvectors $\mathbf{P}_i$ such that:

$$(\mathbf{K} \diamond \mathbf{K}) = \rho\,\mathbf{P} \underset{1\leqslant i\leqslant 3}{\mathrm{diag}}\left(\omega_i^2\right)\,\mathbf{P}^{\mathrm{T}}, \tag{4}$$

where the 3x3 polarization matrix is such that $\mathbf{P} = [\mathbf{P}_1,\,\mathbf{P}_2,\,\mathbf{P}_3]$. Its transpose matrix is noted $\mathbf{P}^{\mathrm{T}}$. The solution is then expressed as follows:

$$\hat{\mathbf{u}}(t) = \frac{1}{\rho}\,\mathbf{P} \underset{1\leqslant i\leqslant 3}{\mathrm{diag}}\left(\frac{\mathbb{h}(\bullet)\sin(\omega_i\bullet)}{\omega_i}\right)\,\mathbf{P}^{\mathrm{T}} * \hat{\mathbf{f}}, \tag{5}$$

where $\mathbb{h}$ is the Heaviside unit step function. Let us now perform a Laplace transform (with parameter $s$) to the solution (5). The Laplace transforms of the ramp and sine functions are $s^{-2}$ and $(1+s^2)^{-1}$, respectively. They are holomorphic on the half-plane $Re(s)>0$, with poles on the imaginary axis.

If the 6D state vector $\hat{\mathbf{H}} = \begin{pmatrix} \hat{\mathbf{U}}^{\mathrm{T}} & \hat{\mathbf{\Sigma}}_z^{\mathrm{T}} \end{pmatrix}^{\mathrm{T}}$ is considered, the solution can be expressed in the dual space $(\mathbf{K}, s)$ as follows:

$$\hat{\mathbf{H}} = \mathbf{M}^{-1}\begin{pmatrix} \mathbf{0} \\ \hat{\mathbf{F}} \end{pmatrix}, \quad \text{where} \quad \mathbf{M} = \begin{pmatrix} \mathbb{i}\,(\mathbf{n}\diamond\mathbf{K}) & \mathbb{I} \\ \rho\,s^2\mathbb{I} + (\mathbf{K}\diamond\mathbf{K}) & \mathbb{O} \end{pmatrix}, \tag{6}$$

$\mathbb{i} = \sqrt{-1}$, $\mathbb{I}$ and $\mathbb{O}$ are the 3-by-3 identity and zero matrices, respectively.

The study of the singularities of $\hat{\mathbf{H}}$ leads to the Christoffel Equation $\det(\mathbf{M}) = 0$. According to the problem geometry, the six solutions of this equation are to be found in terms of complex vertical wavenumbers $k_{z,i}$ $(i = 1\ldots 6)$. Thus, the state vector defined in Eq. (6) can be easily expressed in the $(\mathbf{k}, z, s)$ domain with the notation $\tilde{\mathbf{H}}(z)$. The six complex vertical wavenumbers are sorted by comparing their imaginary parts, such that:

$$\begin{cases} Im(k_{z,i}) > 0, & i{=}1,2,3\,; \\ Im(k_{z,i}) < 0, & i{=}4,5,6\,. \end{cases} \tag{7}$$

Since $Re(s) > 0$, it is proved in Appendix A that the first three partial waves, of vertical wavenumbers with positive imaginary parts, correspond to waves that propagate in the negative $z$ direction, while the others, of vertical wavenumbers with negative imaginary parts, correspond to waves that propagate in the positive $z$ direction. This is an important point because a simple consideration on the imaginary part of $k_{z,i}$ unambiguously separates the fields into upgoing and downgoing waves. This is not the case for harmonic waves, where $Re(s) = 0$ and $Im(s) = \mathbb{i}\,\omega$, for which considerations on direction of energy propagation must be added.

## 3.3 Radiation of a source in an infinite medium: *incident field*

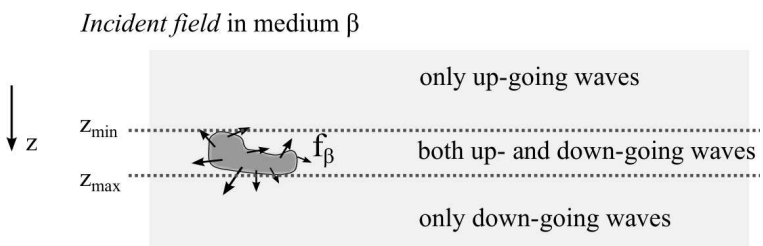


Figure 2: The three regions of space defined by a volume source, in which the *incident field* is calculated respectively with Eq. (8), (11) or (12).

Let us first calculate the radiation of a given source located in the zone defined by $z_{\beta,\min} \leqslant z \leqslant z_{\beta,\max}$, in the layer $\beta$ considered as an infinite space, as shown in Fig. 2. If the source extends beyond the interface $\beta$ (or $\beta+1$), the actual source to be considered is the part of the source located between $z = z_\beta$ and $z = z_{\beta+1}$, although the medium in this section is assumed to be infinite.

As detailed in Appendix A, the radiated field, represented by the state vector $\tilde{\mathbf{H}}_\beta^{inc}$ at the vertical position $z$ in the $(\mathbf{k}, z, s)$-domain, depends on the position of the observation point with respect to the source. It is obtained by convoluting the Green tensor of the unbounded medium by the source term.

As a matter of fact, three cases occur:

- If the observation point is inside the source area ($z_{\min} < z < z_{\max}$),

$$\tilde{\mathbf{H}}_\beta^{\text{inc}}(z) = \sum_{i=1}^{6} \alpha_{\beta,i}(z)\ \boldsymbol{\xi}_{\beta,i} \quad , \tag{8}$$

  where $\boldsymbol{\xi}_{\beta,i}$ is the polarization vector of the mode with vertical wavenumber $k_{z,\beta,i}$ , and $\alpha_{\beta,i}(z)$ represents the contribution of this mode. For upgoing waves ($i$=1, 2, 3), only the part of the source below the observation point is involved:

$$\alpha_{\beta,i}(z) = \int_z^{z_{\max}} \mathbf{g}_{\beta,i}^{\mathrm{T}}(z-\zeta)\, \mathbf{f}_\beta(\zeta) \mathrm{d}\zeta \quad (i{=}1,2,3 \quad \text{and} \quad z < z_{\max}) \ , \tag{9}$$

  where the vector $\mathbf{g}_{\beta,i}$ is related to the Green tensor in the layer $\beta$ (see Appendix A).

  Conversely, for downgoing waves ($i$=4, 5, 6), only the part of the source above the observation point contributes:

$$\alpha_{\beta,i}(z) = \int_{z_{\min}}^{z} \mathbf{g}_{\beta,i}^{\mathrm{T}}(z-\zeta)\, \mathbf{f}_\beta(\zeta) \mathrm{d}\zeta \quad (i{=}4,5,6 \quad \text{and} \quad z > z_{\min}) \ . \tag{10}$$

- If the observation point is above the source ($z \leqslant z_{min}$), only the upgoing waves contribute. Then, the state vector takes the following form:

$$\tilde{\mathbf{H}}_\beta^{\text{inc}}(z) = \sum_{i=1}^{3} \alpha_{\beta,i}\ \exp\left[-\mathrm{i}\, k_{z,\beta,i}\ (z - z_{\min})\right]\ \boldsymbol{\xi}_{\beta,i} \ , \tag{11}$$

  with $\alpha_{\beta,i} = \alpha_{\beta,i}(z_{\min})$.

- If the observation point is below the source $z \geqslant z_{max}$, only downgoing waves are received and the state vector becomes:

$$\tilde{\mathbf{H}}_\beta^{\text{inc}}(z) = \sum_{i=4}^{6} \alpha_{\beta,i}\ \exp\left[-\mathrm{i}\, k_{z,\beta,i}\ (z - z_{\max})\right]\ \boldsymbol{\xi}_{\beta,i} \ , \tag{12}$$

  with $\alpha_{\beta,i} = \alpha_{\beta,i}(z_{\max})$.

Of course, if there is no source in the layer $\beta$, the coefficients $\alpha_{\beta,i}(z)$ are all zero.

At this point, we consider that all the *incident fields* are known in all layers and characterized in the $(\mathbf{k}, z, s)$-domain by $\tilde{\mathbf{H}}_\beta^{\text{inc}}(z)$.

## 3.4 Elastodynamic fields in a layer and interface conditions

Let us now remember that the medium under consideration is bounded ($z_{\beta-1} < z < z_\beta$). The part of the source located in each layer radiates an *incident field* characterized by the state vector $\tilde{\mathbf{H}}_\beta^{\text{inc}}(z)$. The *total field* in the layer is the superposition of this *incident field* with the *reflected field*, resulting from the diffraction at each interface. Consequently, the *reflected field* is completely characterized by six coefficients $a_{\beta,i}$ and the *total field* is expressed as follows:

$$\tilde{\mathbf{H}}_\beta(z) = \tilde{\mathbf{H}}_\beta^{\text{inc}}(z) + \sum_{i=1}^{6} a_{\beta,i}\ \exp\left[-\mathrm{i}\, k_{z,\beta,i}\ (z - z_{\beta,i})\right]\ \boldsymbol{\xi}_{\beta,i} \ , \quad z_\beta < z < z_{\beta+1} \ , \tag{13}$$

where the vertical positions $z_{\beta,i}$ can be arbitrarily chosen [23], as detailed below.

In the upper layer, the *reflected field* contains only upgoing waves:

$$\tilde{\mathbf{H}}_0(z) = \tilde{\mathbf{H}}_0^{\text{inc}}(z) + \sum_{i=1}^{3} a_{0,i} \exp\left[-\mathbb{i}\, k_{z,0,i}\, (z - z_{0,i})\right] \boldsymbol{\xi}_{0,i} \ , \quad z < 0 \ , \tag{14}$$

while in the lower layer, the *reflected field* contains only downgoing waves:

$$\tilde{\mathbf{H}}_{N+1}(z) = \tilde{\mathbf{H}}_{N+1}^{\text{inc}}(z) + \sum_{i=4}^{6} a_{N+11,i} \exp\left[-\mathbb{i}\, k_{z,N+1,i}\, (z - z_{N+1,i})\right] \boldsymbol{\xi}_{N+1,i} \ , \quad z > z_N \ . \tag{15}$$

The $6N{+}6$ coefficients $a_{\beta,i}$ will be determined by rewriting the boundary conditions (2) in the $(\mathbf{k}, z, s)$-domain at the $N{+}1$ interfaces (6 equations at each interface):

$$\tilde{\mathbf{H}}_{\beta+1}\left(z_\beta\right) - \tilde{\mathbf{H}}_{\beta}\left(z_\beta\right) = \begin{pmatrix} \mathbf{0} \\ \tilde{\boldsymbol{\Sigma}}_\beta \end{pmatrix} \ , \tag{16}$$

where the term $\tilde{\boldsymbol{\Sigma}}_\beta$ corresponds to the interface source term $\boldsymbol{\sigma}_\beta(\mathbf{x}, t)$ in this transformed domain.

The arbitrary vertical positions $z_{\beta,i}$ defined in Eq. (13) have been chosen such that: $z_{\beta,i} = z_\beta$ for upgoing waves ($i{=}1, 2, 3$) and $z_{\beta,i} = z_{\beta-1}$ for downgoing waves ($i{=}4, 5, 6$). In agreement with the definition [Eq. (7)], this choice leads to computations only of decreasing exponentials in the layer under consideration. As a consequence, computations are numerically stable irrespective of the frequency-thickness products. The incident wave field radiated by the part of the source located in layer $\beta$ is expressed by Eq. (11) at interface $\beta{-}1$ (upgoing waves over the layer) and by Eq. (12) at interface $\beta$ (downgoing waves under the layer).

The method presented here is known as the *Global matrix* approach (*e.g.*, [14]). However, it is most often stated in the harmonic domain, whereas we are working in the Laplace domain. Note that only the case of elastic layers embedded between two semi-infinite solids is presented above for clarity (giving an invertible linear system of $6N{+}6$ equations with $6N{+}6$ unknowns $a_{\beta,i}$ ). Other types of layer or half-space (fluid, vacuum, *etc.*) give similar equations.

## 3.5 Expression of the solution in the physical domain

Let us first come back to the time domain. From a numerical point of view, this is the most delicate procedure of this method, since an inverse Laplace transform is involved. As shown above, $\tilde{\mathbf{H}}_\beta\left(z\right)$ is holomorphic in the complex half-plane $Re(s) > 0$. Consequently, all its singularities, *i.e.*, poles, branch points and branch cuts, are in the left part of the complex plane, including the imaginary axis. Purely imaginary poles $s = \mathbb{i}\,\omega_0$ correspond to pure guided modes of angular frequency $\omega_0$. Poles with a negative real part are associated to transient leaky guided modes. In fact, although the horizontal wave vector $\mathbf{k}$ is real, the associated slowness vector, such that $\mathbf{S} = \mathbb{i}\, s^{-1}\mathbf{k}$, is complex since the modal frequency is complex, *i.e.*, $Re(s) \neq 0$ (*e.g.*, [20]). In such a description, wave leakage in the upper and lower infinite media of this transient guided wave is described by the imaginary part of the slowness vector, which come from transient effects, due to the real part of $s$.

Under these considerations, the inverse Laplace transform can be calculated, without difficulty, using the Bromwich-Mellin formula:

$$\tilde{\boldsymbol{\eta}}_\beta(z, t) = \frac{\exp(\gamma\, t)}{2\,\pi} \int_{-\infty}^{+\infty} \exp(\mathbb{i}\,\omega\, t)\, \tilde{\mathbf{H}}_\beta(z)\, \mathrm{d}\omega \ , \quad z_{\beta-1} < z < z_\beta \ , \tag{17}$$

where the parameter $\gamma$ is an arbitrary positive constant and where the function $\tilde{\mathbf{H}}_\beta(z)$ is calculated for $s = \gamma{+}\mathbb{i}\,\omega$. From a numerical point of view, the initial inverse Laplace transform is then replaced by a Fourier transform

multiplied by a growing exponential function. In the literature this numerical Laplace inversion is sometimes referred as the Exponential Window Method (*e.g.*, [11]). The principle is to calculate the transient response in the discretized time-interval $[0, t_{\max}]$. The use of discrete Fourier transform results in a periodization of the signals (period $t_{\max}$). Following [11], the usual way to define $\gamma$ is to take $\gamma = m \log(10)\, t_{\max}^{-1}$, which corresponds to periodization effects less than $10^{-m}$. The greater the parameter, the less the periodization effects. Nevertheless, there is a counterpart in increasing $m$ due to the exponential growing factor $\exp(\gamma\, t)$ in Eq. (17). A good compromise is obtained by taking $m$ between 2 and 5.

At this stage, let us come back to the spatial domain, by applying the following 2D inverse Fourier transform:

$$\boldsymbol{\eta}_\beta(\mathbf{x}, z, t) = \frac{1}{4\pi^2} \iint_{\mathbb{R}^2} \exp(-\mathbb{i}\, \mathbf{k} \cdot \mathbf{x})\, \widetilde{\boldsymbol{\eta}}_\beta(z, t)\, \mathrm{d}k_x\, \mathrm{d}k_y\ , \quad z_{\beta-1} < z < z_\beta\ . \tag{18}$$

A 2D inverse Fourier transform, computed by an FFT algorithm, is then used to do this transformation, according to the Nyquist-Shannon sampling theorem. As long as this inverse transform is numerical, the problem is spatially periodic and the solution is valid only as long as the fastest wave front, that propagates at velocity $c^{\theta}_{max}$ in a fixed direction, has not reached the edges of the spatial domain. Therefore, the computational effort is proportional to $k^2_{\max} \times t^3_{\max}$ ($k_{\max} \times t^2_{\max}$ for 2D computations), where $k_{\max}$ denotes the maximum value of the horizontal wave numbers of the source-term, assumed to be bandlimited in wavenumber.

## 3.6 Viscoelastic layers

To take the viscoelastic behavior of each layer into account, a Kelvin-Voigt dissipative model can be used [2]. As a result, the bilinear product $\overset{\beta}{\diamond}$, introduced in Eq. (1), is replaced by $\overset{\beta}{\diamond} + \overset{\beta}{\blacklozenge}\partial_t$ in the time domain. In the Laplace domain, this changing is noted as follows:

$$\overset{\beta}{\diamond} \mapsto \overset{\beta}{\diamond} + s\, \overset{\beta}{\blacklozenge}\ . \tag{19}$$

The new bilinear operator $\overset{\beta}{\blacklozenge}$ defines a 3-by-3 matrix $(\mathbf{a} \overset{\beta}{\blacklozenge} \mathbf{b})$, such that $(\mathbf{a} \overset{\beta}{\blacklozenge} \mathbf{b})_{im} = \eta^{\beta}_{ijkm}\, a_j\, b_k$, where the constants $\eta^{\beta}_{ijkm}$ constitute the viscosity tensor. This model is causal. In addition, in the spectrum domain, *i.e.*, wavevector/frequency domain, it leads to a viscous damping of waves proportional to the square of the frequency [2]. It describes correctly the behavior of polymers in the usual frequency range of NDT and NDE applications. However, it is not accurate for modeling composite materials. Indeed, it has been shown experimentally [10] that wave damping is proportional to frequency in the domain of interest.

In the Laplace domain, such behavior can be described by the following simplistic change:

$$\overset{\beta}{\diamond} \mapsto \begin{cases} \overset{\beta}{\diamond} + \mathbb{i}\, \mathrm{sign}(\mathrm{Im}(s))\, \overset{\beta}{\blacklozenge}\ , & \mathrm{Im}(s) \neq 0\ ; \\ \overset{\beta}{\diamond}\ , & \mathrm{Im}(s) = 0\ . \end{cases} \tag{20}$$

Note that the simplistic model (20) cannot be correct because it does not lead to a holomorphic expression with respect to the complex variable $s$ and does not correspond to a causal model, contrary to the Kelvin-Voigt dissipative model. More refined models can be used but these will be discussed in future articles. Nevertheless, the simplistic model gives acceptable results for the numerical cases presented here. The consequences of such non-physical behavior on the waveform computations will be seen below (see Section 4.3).

Of course in this case, the constants $\eta^{\beta}_{ijkm}$ do not have the same rheological meaning, or the same unit, as those defined in Eq. (19). However, the same variables will be used to define the operator $\overset{\beta}{\blacklozenge}$.

# 4 Numerical results

This section reports some numerical results based on the numerical schemes described above. Three typical plates are analyzed. First, a plate in vacuum consisting of a single layer of a unidirectional fiber composite is considered. Second, the effects of negative propagation in an aluminum plate immersed in water are analyzed. Third, the case of a structure made of 8 unidirectional fiber composite layers stacked together and immersed in water is presented. For all the examples, the computation time will be given for a `C++` language and the computer will be a $1.66\times 2\,GHz$ 64-bit dual core processor with a $2\,Go$ RAM, which is a mid-performance personal computer. Using a newer computer, computation times can easily be divided by ten.

## 4.1 Monolayer plate of carbon-epoxy in vacuum

Within the frequency range of calculations, such a composite material can be considered as an orthotropic homogeneous medium for which the equivalent density is $\rho$=1560 $kg{\cdot}m^{-3}$. The crystallographic directions $\sharp 1$, $\sharp 2$ and $\sharp 3$ correspond to the $x$, $y$ and $z$-axis, respectively. The direction of fibers coincides with the $x$-axis. This composite material has been chosen because it has already been used in some experiments [16, Table 2.3]. Plate thickness is $3.6\,mm$. The homogenized stiffness constants are: $c_{11}$=86.65, $c_{22}$=14.00, $c_{33}$=14.00, $c_{44}$=3.00, $c_{55}$=4.06, $c_{66}$=4.70, $c_{12}$=7.50, $c_{13}$=7.50, $c_{23}$=7.00 $[GPa]$. The source is located on the first interface $z = 0$. In agreement with the experiments, the normal force at this surface, defined in Eq. (1), is modeled by a Gaussian distributed amplitude in the $xy$-plane and coupled to a tone burst signal, such that:

$$\boldsymbol{\sigma}_0(\mathbf{x},t) = \exp\left(-\frac{x^2+y^2}{2\,\sigma^2}\right)\,\sin(\omega_0\,t)\,\exp\left(-\frac{\omega_0^2\,t^2}{2\,n_c^2}\right)\,\begin{pmatrix}0 & 0 & 1\end{pmatrix}^{\mathrm{T}}, \tag{21}$$

with $\omega_0 = 2\,\pi\,f_0$. The other new variables are: the Gaussian aperture $\sigma = 2.4\,mm$, the central frequency $f_0 = 150\,kHz$ and the number of cycles $n_c = 6.5$. First of all, let us examine displacement on the plate surface, *i.e.*, at $z = 0$, for a fixed time $t = 120\,\mu s$. This is a relatively long time for guided waves to propagate over long distances. The matched surface of calculation is such that: $x \in (-1.12\,..\,1.12\,m, 1030]$ and $y \in (-0.39\,..\,0.39\,m, 360]$, where $(v_{\min}\,..\,v_{\max}, n]$ denotes a half-closed discretized interval of $n$ linearly spaced values from $v_{\min}$ to $v_{\max}$. This notation will be used for all sampled variables introduced later on. Thus, the waveforms are observed for $t \in [-22\,..\,228\,\mu s, 150)$. For this 3D problem and for this large plane of analysis, the computation time is $25'$, which is a relatively short time that could be considerably reduced by using a faster computer. As an illustration, Fig. 3-a represents the vertical displacement $u_z$ for a non-dissipative plate. In the frequency range of the emitter and for a composite sample, only four propagating modes can exist. The three fundamental modes $A_0$ (flexural wave), $SH_0$ (horizontal shear wave) and $S_0$ (compressional wave), and the first anti-symmetric mode, usually called $A_1$. The three fastest fronts correspond to the three fundamental modes $A_0$, $SH_0$ and $S_0$. It can be seen in [7] that there is good agreement between the ray theory and the field calculation by using a time-domain modal approach. In this paper, the waveforms have been obtained without modal decomposition but, of course, they correspond exactly to the waveforms obtained in [7], since both are exact solutions of the same problem.

The theory is now compared with experiments reported in [16]. For this, two waveforms are calculated at two different positions on the surface, $(15, 0, 0)$ and $(21.05, 17.68, 0)$, which are identified by the two dots in Fig. 3-a. The associated waveforms are shown in Figs. 3-b and 3-c. Clearly, the agreement between experimental and theory wavefront arrival times is correct, while the amplitudes differ drastically. This is due to wave damping, as is well-known in such composites [10]. To take this effect into account, in agreement with experiments performed in the frequency range associated with the source described by Eq. (21), the viscoelastic model, defined by Eq. (20), is used. The associated viscosity constants of the homogenized solid are: $\eta_{11} = 2.00$, $\eta_{22} = 0.30$, $\eta_{33} = 0.30$, $\eta_{44} = 0.085$, $\eta_{55} = 0.085$, $\eta_{66} = 0.055$, $\eta_{12} = 0.13$, $\eta_{13} = 0.13$, $\eta_{23} = 0.106$ $[kPa{\cdot}rad^{-1}]$. The values of these constants differ from those given in [16]. This is because the values obtained from experiments in this paper, as mentioned, include not only viscosity absorption, but also wave attenuation due to beam diffraction. These two attenuation effects cannot be differentiated experimentally, which is not the case in the present work,

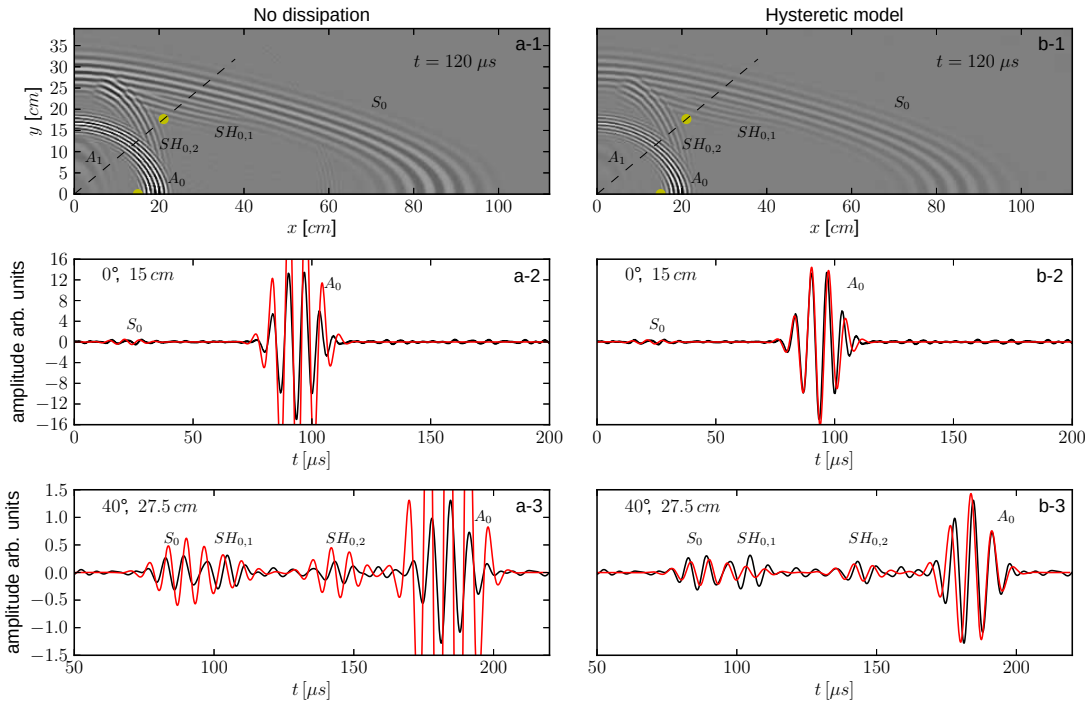


Figure 3: 3D response (vertical displacement) of a monolayer plate of carbon-epoxy to a source located at the top interface ($z = 0$). (a) Non-dissipative medium. (b) Dissipation considered through the hysteretic model. Figures (a)-1 and (b)-1 are views from the top of the plate after a long time, with non-linear gray scale in order to show the low amplitude $SH_0$ and $A_1$ modes. In figures (a)-2,3 and (b)-2,3 the numerical computations (red signals) are compared to the experimental data (black signals) [16].

since beam diffraction is, of course, taken into account by the model. The comparison between theoretical waveforms obtained for a viscoelastic plate and experimental signals is presented in Fig. 3. For the two angles of observation, note the very good agreement between theory and experiment.

## 4.2 Aluminum plate immersed in water

To illustrate the efficiency of the method, it is of interest to calculate the response near the source. To this end, let us consider an aluminum plate immersed in water, which is insonified by a transducer near a ZGV (Zero Group Velocity) condition. Recently, new methods of NDT have been developed taking advantage of the sensitivity to the interface parameters of waves generated in ZGV conditions (*e.g.*, [21]). In our case, the sample thickness is $1\,mm$ and the density is $\rho_1$=2780 $kg{\cdot}m^{-3}$. Using the isotropy relations, all the stiffness constants are deduced from the two independent stiffness constants: $c_{11}$=112.0 and $c_{66}$=27.0 $[GPa]$. The water density is $\rho_0 = 1000\,\mathrm{kg{\cdot}m^{-3}}$ and the sound velocity in water is $1500\,\mathrm{m{\cdot}s^{-1}}$. To observe the ZGV phenomenon clearly, it is important to minimize the wave diffraction effects and to generate a specific Lamb wave precisely at a single frequency. To do this, the simulation of the transducer, which is located in the upper semi-infinite layer, *i.e.*, $\beta = 0$ in Eq. (1), is given by the following function:

$$\mathbf{f}_0\,(x,y,z,t) = \Pi\left[\frac{2\,(z-z_f)}{l\,\sin\theta}\right]\,\exp\left\{-\frac{[x-x_0(z)]^2}{2\,\sigma_x^2}-\frac{y^2}{2\,\sigma_y^2}\right\}\,\sin(\omega_0 t)\,\exp\left(-\frac{\omega_0^2\,t^2}{2\,n_c^2}\right)\,\begin{pmatrix}\sin(\theta)\\0\\\cos(\theta)\end{pmatrix}, \tag{22}$$

where function $\Pi$ is the rectangular function such that $\Pi(\xi) = 1$ if $|\xi| \leqslant 1/2$, and $\Pi(\xi) = 0$ otherwise. The quantity $x_0(z,\theta)$, given by $x_0(z,\theta) = (z - z_f)\,\cot(\theta) - z_f\,\tan(\theta)$, expresses the transducer rotation around its center at position $z_f$, with an additional lateral shift to make the transducer central axis cross the first

| $\theta$ | $f_0$ |
|---|---|
| 2.6° | 3.0 MHz |
| 6.0° | 2.87 MHz |
| 12.7° | 3.0 MHz |

Table 2: The three $(\theta, f_0)$ pairs used in formula (22) to select the backward propagative, zero energy velocity and propagative regimes.

interface at the reference origin defined in Fig. 4. The variable $l$ stands for the length of the transducer. The other variables are the same as those defined in Eq. (21). The parameter values are such that: $\sigma_x = 0.5\,\mathrm{mm}$, $\sigma_y = 10.0\,\mathrm{mm}$, $l = 20.0\,\mathrm{mm}$, $z_f = -6.0\,\mathrm{mm}$ and $n_c = 30$. Because the source $\mathbf{f}_0(x, y, z, t)$ is not proportional to a Gaussian function rotated by the angle $\theta$, it does not model exactly a fixed transducer that is rotated in a fluid. However, results are very close to a unique rotated transducer, and the analytical calculations are simpler. These values correspond to a 3D transducer that generates a quasi-plane wave in $\theta$-direction. For the three cases under consideration, the values of $\theta$ and $f_0$ are given in Table 2. As the angle of incidence increases, these cases correspond to a negative group velocity, the ZGV condition associated to $S_1$ mode, and a positive group velocity respectively. The convolution expressed by Eq. (A.12) is calculated analytically.

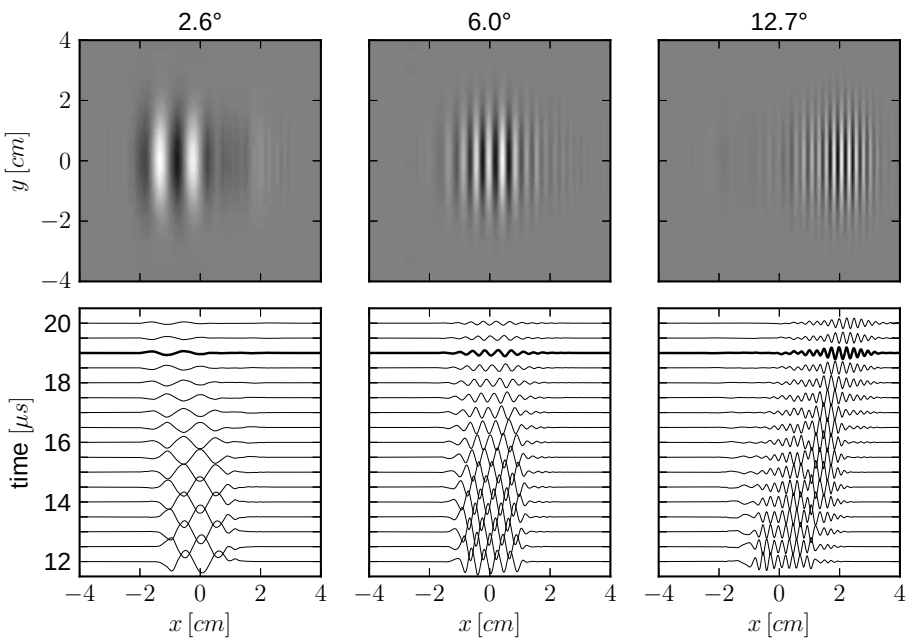


Figure 4: Vertical displacement $u_z$ at the surface of the aluminum plate for the three incidence angles (see Table 2): (a) for $t = 19\,\mu s$ with respect to $x$ and $y$; (b) for $y = 0$ with respect to $x$ and $t$ ; the bold signal corresponds to $t = 19\,\mu s$. From left to right: the backward propagative, zero energy velocity and propagative regimes.

To perform calculations by satisfying the Nyquist criterion, the plate surface has been sampled with $x \in (-60\,..\,60\,mm, 270]$ and $y \in (-60\,..\,60\,mm, 16]$. A zero padding procedure is then applied to the calculated field spectrum to increase the definition of the acoustic fields. The time sampling is such that: $t \in [0\,..\,20\,\mu s, 200)$. For this quasi 2D problem, the calculation time is $5''$. Results are presented in Fig. 4-a, where the vertical displacements at the plate surface, *i.e.* at $z = 0$, are plotted in gray scale, for a fixed time $t = 19\,\mu s$, for the three specified cases. In Fig. 4-b, the same displacement, obtained for $y = 0$ and $z = 0$, is shown for some observation times versus $x$-positions. These graphs start at $12\,\mu s$, since this time is approximately when the incident wave vanishes and the free regime appears. The bold curves correspond to the fixed time of $19\,\mu s$. As expected, it is clearly observed that for the ZGV angle the guided wave does not propagate along the plate, but the transmitted beam is concentrated in the plate under the incident beam, which insonifies the plate around $x = 0$. For the other two angles, the guided waves propagate to the left or to the right in agreement with the

direction of the group velocity. Of course for any angle of incidence, as time increases, the wave amplitude decreases more or less due to radiation leakage into the water.

## 4.3 Plate made of 8 stacked carbon-epoxy layers immersed in water

As a final example, let us inspect the response of a multilayered plate immersed in water. The plate consists of eight stacked carbon-epoxy layers. Each layer is made of the carbon-epoxy composite described in section 4.1, for which viscoelasticity is taken into account by Eq. (20). Its thickness is $3.6\,mm$. The rotation sequence is as follows: [0°/135°/90°/45°/0°/135°/90°/45°].

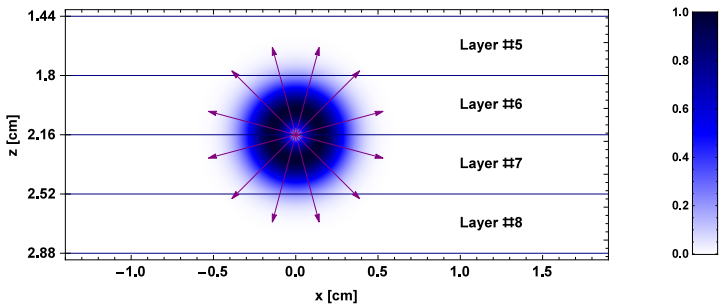


Figure 5: Relative amplitude of the radial source defined by Eq. (23), distributed in length and depth.

To analyze the method possibilities in a new context, the source now represents a line radial impulse located inside the plate. It is distributed horizontally and with depth, as shown in Fig. 5, and is invariant in the $y$-direction. It is centered at depth $z_6 = 21.6\,\mathrm{mm}$ and has a half width of about the thickness of one layer, and therefore extends over four layers.

Although partial waves can exhibit three non-zero components, the problem is then reduced to a 2D space problem. The source expression, in agreement with the definition given in Eq. (1), is such that:

$$\mathbf{f}_\beta(x,y,z,t) = \exp\left[-\frac{x^2+(z-z_6)^2}{2\,\sigma^2}\right]\,\exp\left(-\frac{t^2}{2\,\sigma_t^2}\right)\,\begin{pmatrix} x & 0 & z-z_6 \end{pmatrix}^{\mathrm{T}}, \tag{23}$$

with $\sigma = 1.5\,\mathrm{mm}$ and $\sigma_t = 0.25\,\mu\mathrm{s}$. The value of the parameter $\sigma$ has been chosen to expand the initial force only on the four layers identified by $\beta = 5, 6, 7, 8$. The lateral position is sampled with $x \in (-250\,..\,250\,mm, 370]$. The convolution (A.12) is calculated by using a trapezoidal rule with the following sampling $z \in [15.6\,..\,27.6\,mm, 101]$. From a numerical point of view, because the excitation contains null frequency in this case, it is crucial to deal with viscoelasticity correctly. As a matter of fact, non-respect of causality can provide errors in calculating waveform. The two proposed models do not exhibit the same behavior in this regard, since the model defined by Eq. (20) is not causal, while using Eq. (19) ensures causality. This non-causality comes from the model behavior at low frequencies. Let us sample time by $t \in [0\,..\,40\,\mu s, 240)$. This sampling is optimal to respect the Nyquist-Shannon theorem, using the same rule as before. The waveforms must therefore be well calculated. However, this is not the case for the non-causal model, as shown in Fig. 6-b-1, where waveforms are acquired at position $(0, 0.6)$ in the $xz$-plane. Comparing the non-dissipative plate (solid line) to the dissipative plate (dashed line), reveals substantial differences. Indeed, adverse effects appear for long times, where the signal amplitude increases exponentially. Let us give the explanation. Non respect of causality generates nonzero signal amplitude for low negative times. Consequently, the periodization inherent in spectral discretization creates a copy of this signal at times close to the end of the observation window. After processing with the Laplace inversion algorithm, this contribution is converted to an exponential increase that starts after $30\,\mu s$. To avoid this problem, it is then necessary to increase the observation window as well as the number of points. As a consequence, time is now sampled with $t \in [0\,..\,60\,\mu s, 360)$. The corrected waveform, for which the last $20\,\mu s$ are ignored, is plotted in Fig. 6-b-1 (pointed line). This curve is not identifiable because the observation point

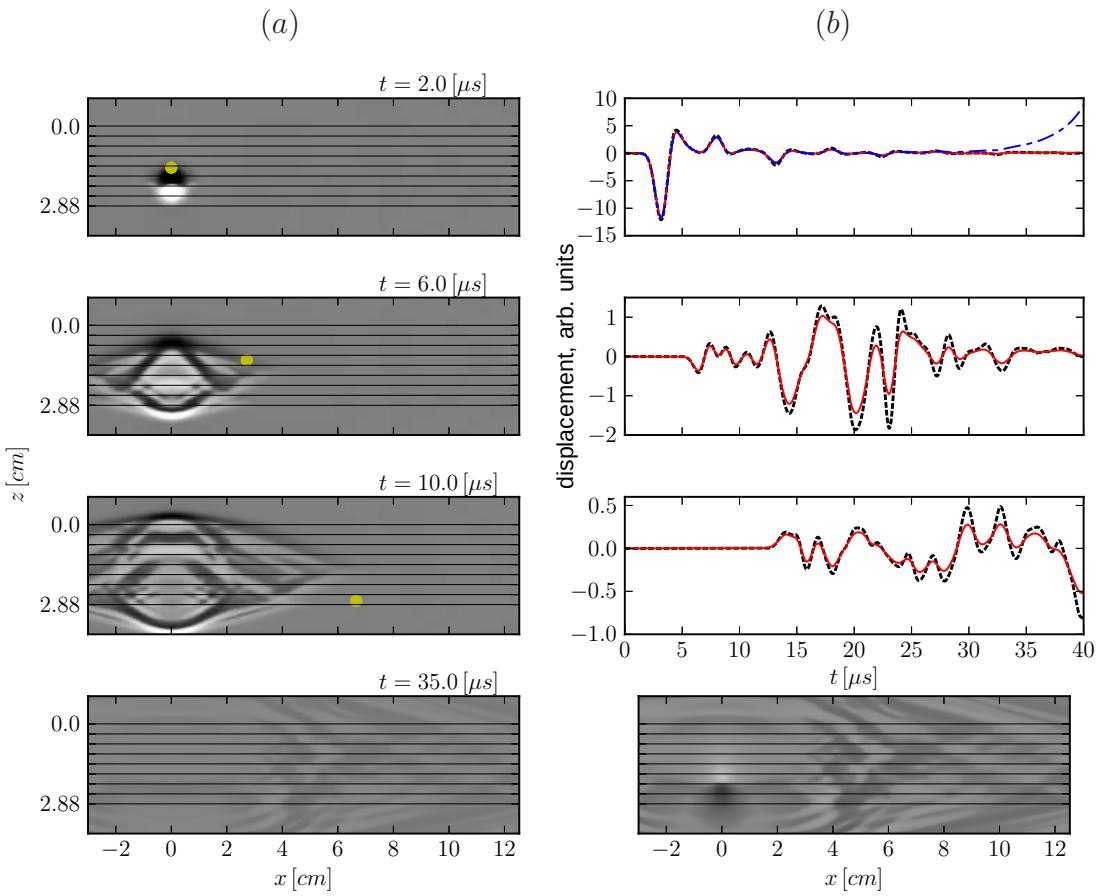


Figure 6: (a) Vertical displacement $u_z$ for $t = 2$, 6, 10 and 35 $\mu s$, for a hysteretic dissipation law and computed with the "increased" time window. (b)-2,3 Signals for the dissipative plate (solid line) and for the non-dissipative plate (dashed line); these signals are computed at the positions indicated by light (yellow) dots in the corresponding figures (a). (b)-1 A third signal plotted with a half-dashed line corresponds to the dissipative plate and the "non-increased" time window, and reveals the behavior of the numerical artifact growing exponentially over time. (b)-4 Vertical displacement uz at $t = 35\,\mu s$, computed using the "non-increased" time window: a numerical artifact can be observed due to non-respect of causality; it is maximal at the location of the source term and at the end of the time window.

is very close to the source, and there is therefore no difference between dissipative and non-dissipative plate responses.

Let us now examine all the results for this dissipative case. They are presented in Figs. 6-a-1 to 6-a-4, where images of vertical displacement $u_z$ are shown at four fixed times ($t$=$2, 6, 10, 35\,\mu s$). As time increases, leaky Lamb waves are seen to form. These guided waves create line wavefronts that radiate energy in water. In addition, for the longest time, the displacement field $u_z$, calculated with the non-matched sampling, is shown in fig. 6-b-4. The artifact mentioned above appears at the location of the source. In order to appreciate the viscoelastic effects better, three waveforms acquired at three fixed positions in the $xy$-plane are plotted in Figs. 6-b-1 to 6-b-3. The three positions are located at: $(0, 0.6)$, $(2.72, 1.25)$ and $(6.66, 2.75)$ and they are identified by light (yellow) dots in Figs. 6-a-1 to 6-a-4. The waveforms obtained for non-dissipative plate (solid line) are compared with those calculated for dissipative plate (dotted line). Clearly, the viscoelastic effects are not really important in comparison with results described in section 4.1. This is because the spectral content is mainly concentrated at low frequencies.

Beyond these expected physical observations, this study illustrates the efficiency of the method which computes, in a reasonable time, the exact acoustic response to an extended source in a multilayered immersed plate. This plate may or may not be viscoelastic. Indeed, with this sampling, to calculate the acoustic field in the $xy$-plane and at any time, $25''$ ($38''$ for viscoelastic plate) are necessary. To conclude this section, it is of great interest to note that, by setting a low value for $\sigma$, the spatial Green tensor can be calculated without any special efforts.

In future work, this possibility will be used to study the diffraction of guided waves by defects.

# 5 Conclusion and prospects

We have adapted an existing method, too little used in ultrasonics, for computing ultrasonic source interactions with multilayered plates, based on time analysis using the Laplace transform. This method provides a useful tool which complements the much used technique based on generalized Lamb wave decomposition. By avoiding mode analysis – which can be problematic in some cases – exact numerical calculations can be made in a relatively short time for immersed plates and viscoelastic layers. Even for 3D cases, numerical costs are relatively low.

These calculations will be used to develop the topological imaging of defects deeply hidden at sub-source positions in multilayered structures. The topological imaging method is based on interactions between two calculated fields, derived from the so-called direct and adjoint problems (*e.g.*, [3, 5, 22], and [25, 27] in geophysics). The tool that we develop will be of prime interest to image defects in 3D composite materials in quasi-real-time, both along the plate and normal to the surface.

There are no specific restrictions concerning the size and the spectrum width of sources, except, of course, Shannon's sampling conditions. As a result, the Green tensor can be calculated without additional efforts and can be used to build a Boundary Element Method. This possibility has been successfully considered for modeling the interaction of planar defects in layered waveguides with a transient incoming wave [15]. An extension is now underway to build a Dirichlet-to-Neumann operator that will enable this tool to be coupled with a commercial Finite Elements software.

# Acknowledgments

This work is jointly funded by "*Region Aquitaine*" and "*CEA-List*", France.

# References

[1] Audoin B., Guilbaud S., *Acoustic waves generated by a line source in a viscoelastic anisotropic medium*, Applied physics letters, **72**(7) (1998) 774-776. DOI 10.1063/1.120889

[2] Auld B.A., Acoustic Fields and Waves in Solids, second ed., Krieger Pub. Co., 1990. ISBN 0894644904

[3] Bonnet M., Guzina B., *Sounding of finite solid bodies by way of topological derivative*, Int. J. Numer. Methods Eng. **61** (2004) 2344–2373. DOI 10.1002/nme.1153

[4] Bonnet-Ben Dhia A.-S., Goursaud B., Hazard C., Prieto A., *Finite element computation of leaky modes in stratified waveguides*, in: Leger A., Deschamps M., (Eds.), *Ultrasonic wave propagation in non-homogeneous media*, Springer proceedings in physics, vol. 128. Springer, Berlin, 2009, pp. 73-86. ISBN 3540891048

[5] Dominguez N., Gibiat V., *Non-destructive imaging using the time domain topological energy method*, Ultrasonics **50** (2010) 367–372. DOI 10.1016/j.ultras.2009.08.014

[6] Ducasse E., Deschamps M., *A nonstandard wave decomposition to ensure the convergence of Debye series for modeling wave propagation in an immersed anisotropic elastic plate*, Wave Motion **49** (2012) 745-764. DOI 10.1016/j.wavemoti.2012.05.001

[7] Ducasse E., Deschamps M., *Time-domain computation of the response of composite layered anisotropic plates to a localized source*, Wave Motion **51** (2014) 1364-1381. DOI 10.1016/j.wavemoti.2014.08.003

[8] Gavrić L., *Computation of propagative waves in free rail using a finite element technique*, J. Sound Vib. **185**(3) (1995) 531-543. DOI doi:10.1006/jsvi.1995.0398

[9] Hayashi T., Inoue D., *Calculation of leaky Lamb waves with a semi-analytical finite element method*, Ultrasonics **54**(6) (2014) 1460-1469. DOI 10.1016/j.ultras.2014.04.021

[10] Hosten B., Deschamps M., Tittmann B. R., *Inhomogeneous wave generation and propagation in lossy anisotropic solids. Application to the characterization of viscoelastic composite materials*, J. Acoust. Soc. Am. **82**(5) (1987) 1763-1770. DOI 10.1121/1.395170

[11] Kausel E. and Roësset J., *Frequency domain analysis of undamped systems*, J. Eng. Mech., **118**(4) (1992) 721-734. DOI 10.1061/(ASCE)0733-9399(1992)118:4(721)

[12] Kausel E., *Thin-layer method: formulation in the time domain*, Int. J. Numer. Meth. Eng. **37**(6) (1994) 927-941. DOI 10.1002/nme.1620370604

[13] Liu G. R., Tani J., Ohyoshi T., Watanabe K. *Characteristic wave surfaces in anisotropic laminated plates*, J. Vib. Acoust., **113**(3) (1991) 279-285. DOI 10.1115/1.2930182

[14] Lowe M. J. S., *Matrix techniques for modeling ultrasonic waves in multilayered media*, IEEE Trans. Ultrason. Ferroelectr. Freq. Control **42**(4) (1995) 525-542. DOI 10.1109/58.393096

[15] Mora P., Ducasse E., Deschamps M., *Interaction of a guided wave with a crack in an embedded multilayered anisotropic plate: global matrix with Laplace transform formalism*, Proceedings of ICU 2015, Physics Procedia **70** (2015) 326-329. DOI 10.1016/j.phpro.2015.08.217

[16] Neau G., Lamb waves in anisotropic viscoelastic plates: study of the wave fronts and attenuation (Ph.D. thesis), Bordeaux I University, 2003.

[17] Park, J. Wave motion in finite and infinite media using the Thin-Layer Method (Ph.D. thesis), Massachusetts Institute of Technology, 2002.

[18] Park J., Kausel E., *Response of layered half-space obtained directly in the time domain, part 1: SH sources*, Bull. Seismol. Soc. Am. **96**(5) (2006) 1795-1809. DOI 10.1785/0120050247

[19] Phinney R. A., *Theoretical calculation of the spectrum of first arrivals in layered elastic mediums*, J. Geophys. Res. **70**(20) (1965) 5107-5123. DOI 10.1029/JZ070i020p05107

[20] Poncelet 0., Deschamps M. , *Lamb waves generated by complex harmonic inhomogeneous plane waves*, J. Acoust. Soc. Am. **102**(1) (1997) 292-300. DOI 10.1121/1.419752

[21] Prada C., Clorennec D., Royer D., *Local vibration of an elastic plate and zero-group velocity Lamb modes*, J. Acoust. Soc. Am. **124**(1) (2008) 203-212. DOI 10.1121/1.2918543

[22] Rodriguez S., Deschamps M., Castaings M., Ducasse E., *Guided wave topological imaging of isotropic plates*, Ultrasonics **54** (2014) 1880–1890. DOI 10.1016/j.ultras.2013.10.001

[23] Schmidt H., Tango C., *Efficient global matrix approach to the computation of synthetic seismograms*, Geophys. J. Roy. Astr. Soc. **84**(2) (1986) 331-359. DOI 10.1111/j.1365-246X.1986.tb04359.x

[24] Stroh A.N., *Steady state problems in anisotropic elasticity*, J. Math. Phys. **41** (1962) 77–103. DOI 10.1002/sapm196241177

[25] Tarantola A., *Inversion of seismic reflection data in the acoustic approximation*, Geophysics **49**(8) (1984) 1259–1266. DOI 10.1190/1.1441754

[26] Velichko A., Wilcox P. D., *Modeling the excitation of guided waves in generally anisotropic multilayered media*, J. Acoust. Soc. Am. **121**(1) (2007) 60-69. DOI 10.1121/1.2390674

[27] Virieux J., Operto S., *An overview of full-waveform inversion in exploration geophysics*, Geophysics **74**(6) (2009) WCC127–WCC152. DOI 10.1190/1.3238367

[28] Weaver R. L., Sachse W. and Niu L., *Transient ultrasonic waves in a viscoelastic plate: Theory*, J. Acoust. Soc. Am. **85**(6) (1989) 2255-2261. DOI 10.1121/1.397770

# Appendix A On the use of the Green tensor of an infinite anisotropic medium, in the $(\mathbf{k}, z, s)$-domain

## A.1 General considerations

A source emitting in the medium labeled $\beta$ and located between $z = z_{\min}$ and $z = z_{\max}$ is represented by the following term:

$$\mathbf{f}_\beta(\mathbf{x}, z, t) = \int_{z_{\min}}^{z_{\max}} \delta(z-\zeta)\, \mathbf{f}_\beta(\mathbf{x}, \zeta, t)\, \mathrm{d}\zeta \ . \tag{A.1}$$

In the $(\mathbf{k}, z, s)$-domain, the response of the medium, considered as an infinite space, is expressed as follows:

$$\tilde{\mathbf{U}}(z) = \int_{z_{\min}}^{z_{\max}} \tilde{\mathbf{G}}(z-\zeta)\, \tilde{\mathbf{F}}_\beta(\zeta)\, \mathrm{d}\zeta \ . \tag{A.2}$$

where $\tilde{\mathbf{G}}$ denotes the Green tensor.

In the $(\mathbf{k}, k_z, s)$-domain, the Green tensor is simply expressed as follows:

$$\hat{\mathbf{G}} = \hat{\mathbf{A}}^{-1}\,, \text{ where } \hat{\mathbf{A}} = \big[\rho\, s^2 \mathbb{I} + (\mathbf{K}\diamond\mathbf{K})\big] = \big\{\rho\, s^2 \mathbb{I} + (\mathbf{k}\diamond\mathbf{k}) + k_z\big[\,(\mathbf{n}\diamond\mathbf{k}) + (\mathbf{k}\diamond\mathbf{n})\,\big] + k_z^2\,(\mathbf{n}\diamond\mathbf{n})\big\}\ , \tag{A.3}$$

and is necessarily holomorphic on the complex half-plane $Re(s) > 0$.

## A.2 Green tensor in the $(\mathbf{k}, z, s)$-domain

The following Fourier transform yields the Green tensor in the $(\mathbf{k}, z, s)$-domain:

$$\tilde{\mathbf{G}}(z) = \frac{1}{2\,\pi} \int_{-\infty}^{+\infty} \exp(-\mathrm{i}\, k_z\, z)\ \hat{\mathbf{A}}(\mathbf{k}, k_z, s)^{-1}\ \mathrm{d}k_z, \tag{A.4}$$

The determinant of the matrix $\hat{\mathbf{A}}(\mathbf{k}, k_z, s)$ defined by Eq. (A.3) is a polynomial function of $s^2$ (third degree) and $k_z$ (sixth degree) with real coefficients and is usually named the "*Christoffel polynomial*". Consequently, the Green tensor $\hat{\mathbf{G}}(\mathbf{k}, \bullet, s)$ has exactly six poles $k_{z,i}(\mathbf{k}, s)$ in the complex plane, which are continuous functions of the Laplace variable $s$.

If $Re(s) > 0$, $k_{z,i}(\mathbf{k}, s)$ can never be a real number because the matrix $\hat{\mathbf{A}}(\mathbf{k}, k_z, s) - \rho\, s^2 \mathbb{I}$ is real-valued symmetric positive-definite if $k_z$ is also a real number.

If $s$ is a positive real number, the matrix $\hat{\mathbf{A}}(\mathbf{k}, k_z, s)$ is real-valued symmetric positive-definite, and the vertical wavenumbers $k_{z,i}(\mathbf{k}, s)$ necessarily appear in complex conjugate pairs. Thus, there are three wavenumbers with a positive imaginary part ($i$=1, 2, 3), and three with a negative imaginary part ($i$=4, 5, 6).

This latter property can be extended to $s$ values in the half-plane $Re(s) > 0$ because the imaginary part of $k_{z,i}(\mathbf{k}, s)$ is a continuous function of $s$ which cannot be zero on the complex half-plane $Re(s) > 0$.

Furthermore, $\hat{\mathbf{G}}(\mathbf{k}, k_z, s) \underset{k_z \to \pm\infty}{\sim} k_z^{-2}\, (\mathbf{n} \diamond \mathbf{n})^{-1}$.

Accordingly, by applying the residue theorem on an half-disk of radius tending to infinity, the Green tensor can be expressed as follows:

$$\tilde{\mathbf{G}}(z) = \left| \begin{array}{lll} \displaystyle\sum_{i=1}^{3} \exp(-\mathbb{i}\, k_{z,i}\, z)\, \tilde{\mathbf{B}}_i & \text{if} \quad z < 0 & \text{(upgoing waves)} \\ \displaystyle\sum_{i=4}^{6} \exp(-\mathbb{i}\, k_{z,i}\, z)\, \tilde{\mathbf{B}}_i & \text{if} \quad z > 0 & \text{(downgoing waves)} \end{array} \right. \tag{A.5}$$

Furthermore, if the Green tensor associated to the vertical stress is introduced as follows:

$$\tilde{\mathbf{T}}(z) = -\mathbb{i}\, (\mathbf{n} \diamond \mathbf{k})\, \tilde{\mathbf{G}}(z) + (\mathbf{n} \diamond \mathbf{n})\, \partial_z \tilde{\mathbf{G}}(z)\ ; \tag{A.6}$$

it can be demonstrated that $\tilde{\mathbf{G}}$ and $\tilde{\mathbf{T}}$ satisfy the following ordinary differential system:

$$\partial_z \begin{bmatrix} \tilde{\mathbf{G}}(z) \\ \tilde{\mathbf{T}}(z) \end{bmatrix} = \underbrace{\begin{bmatrix} \mathbb{i}\, (\mathbf{n}\diamond\mathbf{n})^{-1}(\mathbf{n}\diamond\mathbf{k}) & (\mathbf{n}\diamond\mathbf{n})^{-1} \\ \rho\, s^2\, \mathbb{I} + (\mathbf{k}\diamond\mathbf{k}) - (\mathbf{k}\diamond\mathbf{n})\, (\mathbf{n}\diamond\mathbf{n})^{-1}(\mathbf{n}\diamond\mathbf{k}) & \mathbb{i}\, (\mathbf{k}\diamond\mathbf{n})\, (\mathbf{n}\diamond\mathbf{n})^{-1} \end{bmatrix}}_{\mathcal{S}} \begin{bmatrix} \tilde{\mathbf{G}}(z) \\ \tilde{\mathbf{T}}(z) \end{bmatrix} - \delta(z) \begin{bmatrix} \mathbb{O} \\ \mathbb{I} \end{bmatrix} \tag{A.7}$$

Consequently, the six complex vertical wavenumbers $k_{z,i}$ are the eigenvalues of the matrix $\mathbb{i}\,\mathcal{S}$, proportional to the so-called "*Stroh Matrix*" [24]. They are associated to eigenvectors $\boldsymbol{\xi}_i$ such that:

$$\begin{bmatrix} \tilde{\mathbf{G}}(z) \\ \tilde{\mathbf{T}}(z) \end{bmatrix} = \left| \begin{array}{lll} \displaystyle\sum_{i=1}^{3} \exp(-\mathbb{i}\, k_{z,i}\, z)\, \boldsymbol{\xi}_i\, \mathbf{q}_i^{\mathrm{T}} & \text{if} \quad z < 0 & \text{(upgoing waves)} \\ \displaystyle\sum_{i=4}^{6} \exp(-\mathbb{i}\, k_{z,i}\, z)\, \boldsymbol{\xi}_i\, \mathbf{q}_i^{\mathrm{T}} & \text{if} \quad z > 0 & \text{(downgoing waves)} \end{array} \right. \tag{A.8}$$

where the 3D vectors $\mathbf{q}_i$ satisfy the following invertible linear system of 18 equations with 18 unknowns:

$$\sum_{i=1}^{3} \boldsymbol{\xi}_i\, \mathbf{q}_i^{\mathrm{T}} - \sum_{i=4}^{6} \boldsymbol{\xi}_i\, \mathbf{q}_i^{\mathrm{T}} = \begin{bmatrix} \mathbb{O} \\ \mathbb{I} \end{bmatrix}\ . \tag{A.9}$$

## A.3 Response to an extended source

The response to an extended source located between $z = z_{\min}$ and $z = z_{\max}$ is obtained by combining Eqs. (A.2) and (A.8):

$$\begin{aligned} \tilde{\mathbf{H}}(z) = \begin{bmatrix} \tilde{\mathbf{U}}(z) \\ \tilde{\boldsymbol{\Sigma}}_z(z) \end{bmatrix} = & \int_{\max(z,z_{\min})}^{z_{\max}} \sum_{i=1}^{3} \exp[-\mathbb{i}\, k_{z,i}\, (z-\zeta)]\, \boldsymbol{\xi}_i\, \mathbf{q}_i^{\mathrm{T}}\, \tilde{\mathbf{F}}_\beta(\zeta)\, \mathrm{d}\zeta + \\ & \int_{z_{\min}}^{\min(z,z_{\max})} \sum_{i=4}^{6} \exp[-\mathbb{i}\, k_{z,i}\, (z-\zeta)]\, \boldsymbol{\xi}_i\, \mathbf{q}_i^{\mathrm{T}}\, \tilde{\mathbf{F}}_\beta(\zeta)\, \mathrm{d}\zeta\ . \end{aligned} \tag{A.10}$$

An observation point between $z_{\min}$ and $z_{\max}$ receives both upgoing waves from the part of the source below the point and downgoing waves from the part of the source above the point:

$$\tilde{\mathbf{H}}(z) = \sum_{i=1}^{6} \alpha_i(z)\, \boldsymbol{\xi}_i\ , \quad z_{\min} < z < z_{\max}\ , \tag{A.11}$$

where

$$\alpha_i(z) = \left| \begin{array}{ll} \mathbf{q}_i^{\mathrm{T}} \displaystyle\int_z^{z_{\max}} \exp[-\mathbb{i}\, k_{z,i}\,(z-\zeta)]\, \tilde{\mathbf{F}}_\beta(\zeta)\, \mathbb{d}\zeta\ , & i{=}1,2,3\ ; \\ \mathbf{q}_i^{\mathrm{T}} \displaystyle\int_{z_{\min}}^{z} \exp[-\mathbb{i}\, k_{z,i}\,(z-\zeta)]\, \tilde{\mathbf{F}}_\beta(\zeta)\, \mathbb{d}\zeta\ , & i{=}4,5,6\ . \end{array} \right. \tag{A.12}$$

The $\alpha_i(z)$ term represents the contribution to the wave number $i$ of the part of the source either below the observation point (upgoing waves, $i{=}1,2,3$) or above the observation point (downgoing waves, $i{=}4,5,6$).

For an observation point above the source ($z \leqslant z_{\min}$), only upgoing waves contribute to the radiated field:

$$\tilde{\mathbf{H}}(z) = \sum_{i=1}^{3} \alpha_i(z_{\min})\, \exp[-\mathbb{i}\, k_{z,i}\,(z - z\mathrm{min})]\, \boldsymbol{\xi}_i\ , \tag{A.13}$$

while for an observation point below the source ($z \geqslant z_{\max}$), only downgoing waves contribute:

$$\tilde{\mathbf{H}}(z) = \sum_{i=4}^{6} \alpha_i(z_{\max})\, \exp[-\mathbb{i}\, k_{z,i}\,(z - z\mathrm{max})]\, \boldsymbol{\xi}_i\ . \tag{A.14}$$